A PAR-1–dependent orientation gradient of dynamic microtubules directs posterior cargo transport in the *Drosophila* oocyte

Richard M. Parton,[1] Russell S. Hamilton,[1] Graeme Ball,[1] Lei Yang,[2] C. Fiona Cullen,[3] Weiping Lu,[2] Hiroyuki Ohkura,[3] and Ilan Davis[1]

[1]Department of Biochemistry, University of Oxford, Oxford OX1 3QU, England, UK
[2]Department of Physics, Heriot-Watt University, Edinburgh EH14 4AS, Scotland, UK
[3]Wellcome Trust Centre for Cell Biology, University of Edinburgh, Edinburgh EH9 3JR, Scotland, UK

Cytoskeletal organization is central to establishing cell polarity in various cellular contexts, including during messenger ribonucleic acid sorting in *Drosophila melanogaster* oocytes by microtubule (MT)-dependent molecular motors. However, MT organization and dynamics remain controversial in the oocyte. In this paper, we use rapid multichannel live-cell imaging with novel image analysis, tracking, and visualization tools to characterize MT polarity and dynamics while imaging posterior cargo transport. We found that all MTs in the oocyte were highly dynamic and were organized with a biased random polarity that increased toward the posterior. This organization originated through MT nucleation at the oocyte nucleus and cortex, except at the posterior end of the oocyte, where PAR-1 suppressed nucleation. Our findings explain the biased random posterior cargo movements in the oocyte that establish the germline and posterior.

Introduction

The organization of the cytoskeleton is central to establishing cell polarity in oocytes and somatic cells in a variety of animals (Etienne-Manneville and Hall, 2003; Steinhauer and Kalderon, 2006) and has been a subject of considerable interest (Steinhauer and Kalderon, 2006). The general consensus has been that generating a strong intracellular polarity always requires the cytoskeleton to become highly polarized. In the *Drosophila melanogaster* oocyte, establishing the germline and future axes of the embryo depends critically on molecular motor-based transport of mRNA cargoes along microtubules (MTs; Brendza et al., 2000; Palacios and St Johnston, 2002; Tekotte and Davis, 2002; Serbus et al., 2005). For example, *bcd* (*bicoid*) and *grk* (*gurken*) mRNA, which are essential to establish the anteroposterior and dorsoventral body axes, are transported by the MT minus end–directed Dynein motor to the anterior cortex and dorsoventral corner, respectively (St Johnston et al., 1989; Roth et al., 1995). In a similar way, the plus end–directed motor Kin1 (Kinesin-1; Brendza et al., 2000) transports mRNA encoding the posterior axis and germline determinant *osk* (oskar; Ephrussi et al., 1991) to the posterior. Similar mechanisms of transporting mRNAs operate in a wide range of polarized cell types, including neurons and fibroblast cells, in which mRNA localization targets synthesis of proteins to their site of function (St Johnston, 2005; Czaplinski and Singer, 2006; Rodriguez et al., 2008; Meignin and Davis, 2010; Weil et al., 2010).

The prevailing view of MT organization in the *Drosophila* oocyte is of a relatively stable network with a strong bias in MT orientation toward the posterior. This notion is largely based on static analysis of MT organization in fixed material (Theurkauf et al., 1992; Cha et al., 2002; Januschke et al., 2006) or using Tau-GFP to mark all MTs in living egg chambers (Micklem et al., 1997). Furthermore, the final distributions of cargoes or modified motor protein reporters have been used to infer indirectly the overall distribution of plus or minus ends (Clark et al., 1994, 1997; Micklem et al., 1997; Cha et al., 2002; Becalska and Gavis, 2010). These numerous studies have led to the formulation of three main conflicting models for the organization of the MT network that directs the polarized transport of RNA

R.S. Hamilton and G. Ball contributed equally to this paper.
Correspondence to Ilan Davis: ilan.davis@bioch.ox.ac.uk
Abbreviations used in this paper: fps, frame per second; MT, microtubule.

The Rockefeller University Press $30.00
J. Cell Biol. Vol. 194 No. 1 121–135
www.jcb.org/cgi/doi/10.1083/jcb.201103160

cargoes (Clark et al., 1994, 1997; Theurkauf and Hazelrigg, 1998; Cha et al., 2001, 2002; Januschke et al., 2006; Zimyanin et al., 2008). In the simplest model, MTs are highly polarized along the anteroposterior axis, such that minus ends are located at the anterior with plus ends extending toward the posterior (Clark et al., 1994, 1997), and MTs show an overall gradient of decreasing density from anterior to posterior (Micklem et al., 1997). In the second model, MTs are nucleated around the cortex of the oocyte, with the exception of the posterior, leading to plus ends of MTs being directed toward the center (Cha et al., 2002; Serbus et al., 2005). A variation on this model is one in which the MTs are nucleated predominantly from the oocyte nucleus (Januschke et al., 2006) rather than all over the anterior. The third model proposes that a nonpolarized MT network carries out transport along specifically oriented, biochemically and functionally distinct MT subpopulations. Although posttranslational modifications of MTs, such as acetylation, detyrosination, and glutamylation, that could account for this are known from other systems (Reed et al., 2006; Dunn et al., 2008; Hammond et al., 2008; Bartolini and Gundersen, 2010), there is currently no clear evidence to identify such subpopulations in the *Drosophila* oocyte from early to mid-oogenesis.

The limitations of our understanding of MT organization in the oocyte were brought into sharp focus when *osk* mRNA was shown to move at the posterior of the oocyte in a biased random walk (Zimyanin et al., 2008), which could not be explained well by any of the prevailing models, leading to the possibility that the MTs themselves could adopt such a biased random distribution of polarity. However, this hypothesis could not be tested directly with the available data and methods of analysis of MT organization. Moreover, to date, the different models for MT organization have not been definitively tested because of a lack of direct studies of the dynamics and orientations of the individual MTs that make up the MT network in the oocyte. This is mostly because of technical difficulties in recording the complexity of MT architecture and dynamics in such a large cell in vivo but also stems from the inability to fix MTs instantly without some degree of depolymerization. These limitations apply to oocytes and somatic cells in other systems, and in general, there have not been any suitable imaging and image analysis tools for the description of global MT polarity.

Here, we distinguish between the prevailing models for MT organization and test whether there is an underlying biased random distribution of MT plus ends toward the posterior that could account for the observed posterior cargo transport. We achieve this by characterizing the relationship between cargo movements and MT distribution and by mapping global MT orientation in living oocytes using the MT plus end marker EB1-GFP (Shimada et al., 2006) together with state of the art imaging and development of novel image analysis, statistical, and visualization methods. We find a highly dynamic MT network, upon which we observe cargo movements that, despite its apparent randomness, shows an underlying directionality bias that increases from anterior to posterior. Our observations provide a good explanation for why *osk* mRNA and Staufen protein move in a biased random walk to the posterior. We find no evidence of stable MT subpopulations. Our experiments demonstrate MT nucleation from the anterolateral cortex in a gradient of diminishing abundance to a complete absence from the posterior, where we show that MT nucleation is suppressed by PAR-1. We propose that subtleties in the organization of a highly dynamic MT network are a widespread feature of cells displaying complex behaviors and changes in polarity.

Results

Dynamic MTs form a network extending from the anterior to the posterior of stage 9 oocytes

Transport by the MT plus end–directed motor Kin1 has been shown to be responsible for posterior cargo transport in the *Drosophila* oocyte (Brendza et al., 2000, 2002; Cha et al., 2001). It was subsequently proposed that MTs are absent from the posterior so that Kin1 only transports cargoes to the center of the oocyte, and cargo arrives at its final destination by diffusion and posterior capture (Cha et al., 2002). To test this hypothesis directly, we investigated the distribution of MTs in living oocytes using sensitive rapid time-lapse imaging of Tau-GFP, which marks all MTs along their entire length. We found that, at the anterior, the MT network consisted of a dense, tight mesh of interleaved filaments throughout the cytoplasm (Fig. 1, A and A′). In contrast, at the posterior, MTs are much less abundant but extend along the cortex into the extreme posterior in early to mid-stage 9 oocytes (Fig. 1 A′′). We interpret the previous failure to detect MTs at the posterior as being caused by posterior MT depolymerization during fixation and the microscope methods used at the time being too insensitive to detect the sparse MTs that extend into the posterior.

There has been a general implicit assumption that cargo transport occurs on stable networks of highly polarized MTs in the oocyte, but this has not been addressed previously. To determine whether or not the posterior MTs are stable, we performed time-lapse imaging to follow turnover of Tau-GFP–labeled MTs (Fig. 1 B and Video 1). We measured the persistence of individual MTs and related this to criteria for stability used in other cell types (Infante et al., 2000; Sousa et al., 2007). We found that, toward the posterior, nearly all MTs examined persisted for <6 min (95%; $n = 42$), whereas the maximum time of persistence observed for the sampled population was 10 min. In previous studies in tissue-culture cells, the criteria for dynamic MTs is persistence for <15 min (Infante et al., 2000). We conclude that MTs within the oocyte are unstable at the posterior.

We then investigated whether MTs are dynamic throughout the whole oocyte. To overcome the technical difficulty that Tau-GFP labeling is too dense in the anterior to assess the dynamics of individual MTs, we covisualized Tau-GFP MTs with EB1-mCherry, which labels extending plus ends of MTs. Surprisingly, EB1 foci were found throughout the oocyte, the anterior MT meshwork being particularly densely populated with multiple trajectories, running in different orientations, both parallel and antiparallel along existing MTs (Fig. 2 A and Video 2). The mean rate of MT extension was 0.17 µm/s (±0.01 SEM; maximum rate observed was 0.6 µm/s; $n = 4$ oocytes), which is comparable with the rates of extension in tissue-culture

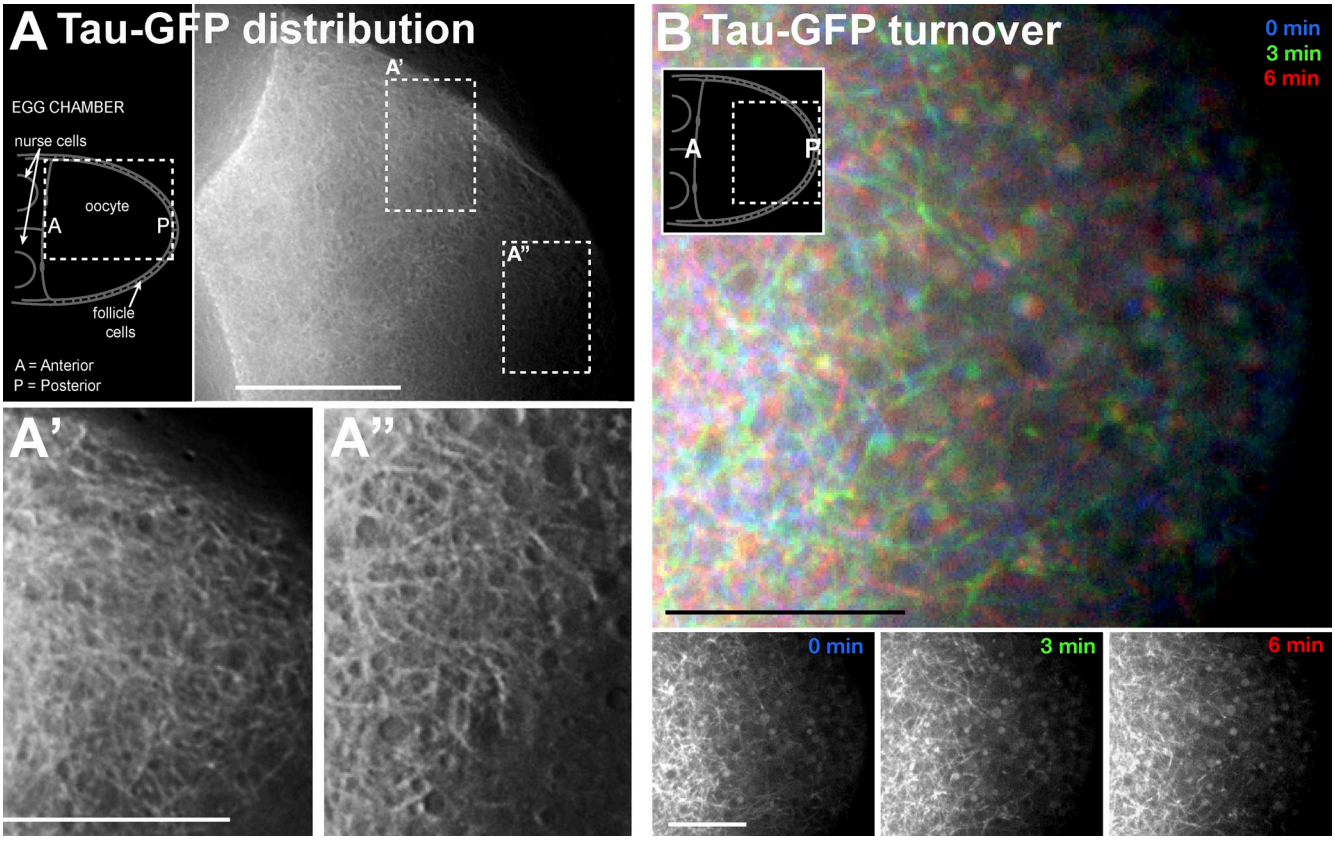

Figure 1. **A dynamic network of MTs extends throughout the oocyte posterior.** Also see Video 1. (A–A′′) Tau-GFP–labeled MT in a living stage 9 oocyte. (A) Overview from anterior to posterior (projected 10-µm z series at reduced magnification) showing the gradient in MT density. (A′ and A′′) Two regions at increased magnification (100× 1.4 NA oil objective) showing the tight dense network of MTs toward the anterior and the more sparse network of MTs extending into the extreme posterior (projected 4-µm z series, which were contrasted individually to display the MT present). (B) Comparison of the Tau-GFP–labeled MT distribution at three time points merged as an RGB image to highlight the changes. The individual channels are shown below. Inserted diagrams in A and B show the orientation of the *Drosophila* egg chamber and the portion of the oocyte imaged. Throughout the images, the convention is posterior to the right. Bars: (A) 25 µm; (A′ and B) 10 µm.

cells (Perez et al., 1999). To determine what proportion of MTs were actively dynamic, we quantified the relationship between Tau and EB1 labeling. Toward the posterior, where it was possible to clearly identify individual MTs (Fig. 2 B and Video 3), we find that EB1 and Tau both mark the same population of dynamically extending MTs (80% association; n = 452 MTs; 20% of MTs did not exhibit extension within the plane of focus and were not associated with an extending EB1 trajectory). We conclude that the vast majority of MTs are dynamic in the oocyte.

To further investigate the dynamic nature of the MTs, we tested for the presence of posttranslational tubulin modifications, which is an accepted indicator of MT stabilization (Hammond et al., 2008). We performed immunolabeling for acetylated and glutamylated tubulin. Our results show that, although MTs in follicle cells, which are known to show increased resistance to MT depolymerization treatments (Januschke et al., 2006), contain modified tubulin, the oocyte MTs lack modified tubulin (Fig. S1). These observations are consistent with our demonstration of dynamic MTs in the oocyte. Considering our results so far, we conclude that MTs extend into the extreme posterior of the oocyte and are highly dynamic and unstable throughout the whole oocyte. This raises the question of whether Kin1-dependent cargo transport is supported on these dynamic unstable MTs.

Posterior-directed cargoes are actively transported on a network of dynamic MTs at the posterior of the oocyte

To determine directly whether the dynamic MTs we observe extending into the posterior are used for posterior cargo transport, we covisualized MTs and Staufen-RFP at high resolution during early to mid-stage 9, at the peak of active cargo redistribution from the center of the oocyte to the posterior (Fig. 3). We found a clear overlap between posterior MTs and actively transported Staufen-RFP particles (Fig. 3 A). Quantifying the relationship between MTs and Staufen particles, we found that 84% of Staufen-RFP particles (n = 25) that showed directed transport could be directly observed moving on Tau-GFP–labeled MTs (Fig. 3 B and Video 4). We followed individual MTs upon which cargo movement was observed and found them to be unstable (persisted <10 min). Moreover, we observed several instances of MTs depolymerizing very shortly after the particle transit (Fig. 3 B, bottom; and Video 5). We conclude that the individual dynamic MTs present at the posterior are genuine conduits for posterior cargo transport.

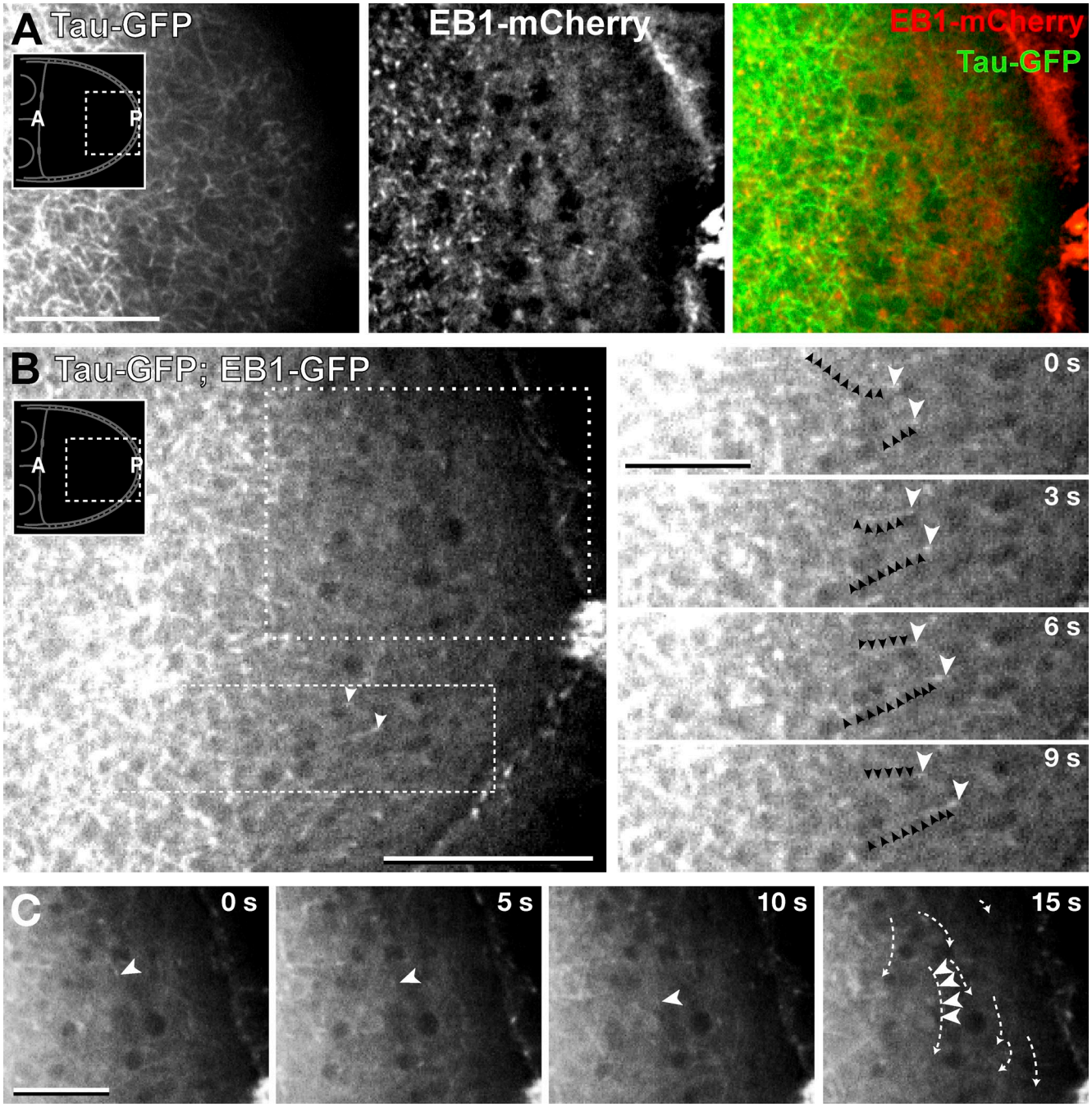

Figure 2. **EB1 tracks the plus ends of dynamic MTs throughout the oocyte.** (A) Dual-channel imaging of Tau-GFP and EB1-mCherry expressed in the same oocyte reveals the association of EB1 with the plus ends of Tau-labeled MTs throughout the oocyte (Video 2). Note that the density of EB1 tracks matches the gradient in MT density from the anterior to posterior of the oocyte and that individual MTs extend well into the extreme posterior. Insets show the portion of the oocyte imaged and its orientation. (B) Tau-GFP and EB1-GFP expressed in the same oocyte allow individual extending MTs to be followed (Video 3). (right) Detail of two individual MTs extending (black arrowheads mark the length of the MT, and white arrowheads mark the extending plus end) taken from the region shown in B (bottom dashed box and white arrowheads). A series of four time points is shown. (C) A time course sequence from a time-lapse video showing that at the extreme posterior, MTs tend to bend round the cortex back on themselves. The images correspond to the top large region in B outlined with white dots. White arrowheads highlight a single extending MT, whereas at the final time point, several MTs are indicated with dashed arrows, which is drawn from Video 3. A, anterior; P, posterior. Bars: (A and B, left) 15 µm; (B, right; and C) 7.5 µm.

To determine whether transport on the dynamic MTs could make a significant contribution to the net movement of the posterior-directed cargo, we analyzed the proportion of particles that display active transport. We found that, at any given time, 14.1% of Staufen-RFP cargo particles identified show directed transport. The remainder were either stationary or exhibited very small nondirectional displacements (n = 1,080 particles; unpublished data). Our results suggest that at stage 9, active transport rather than diffusion or bulk cytoplasmic flow is the major contributor to cargo localization to the posterior. We conclude that transport along dynamic MTs makes a significant contribution to the movement of posterior cargo, but these findings

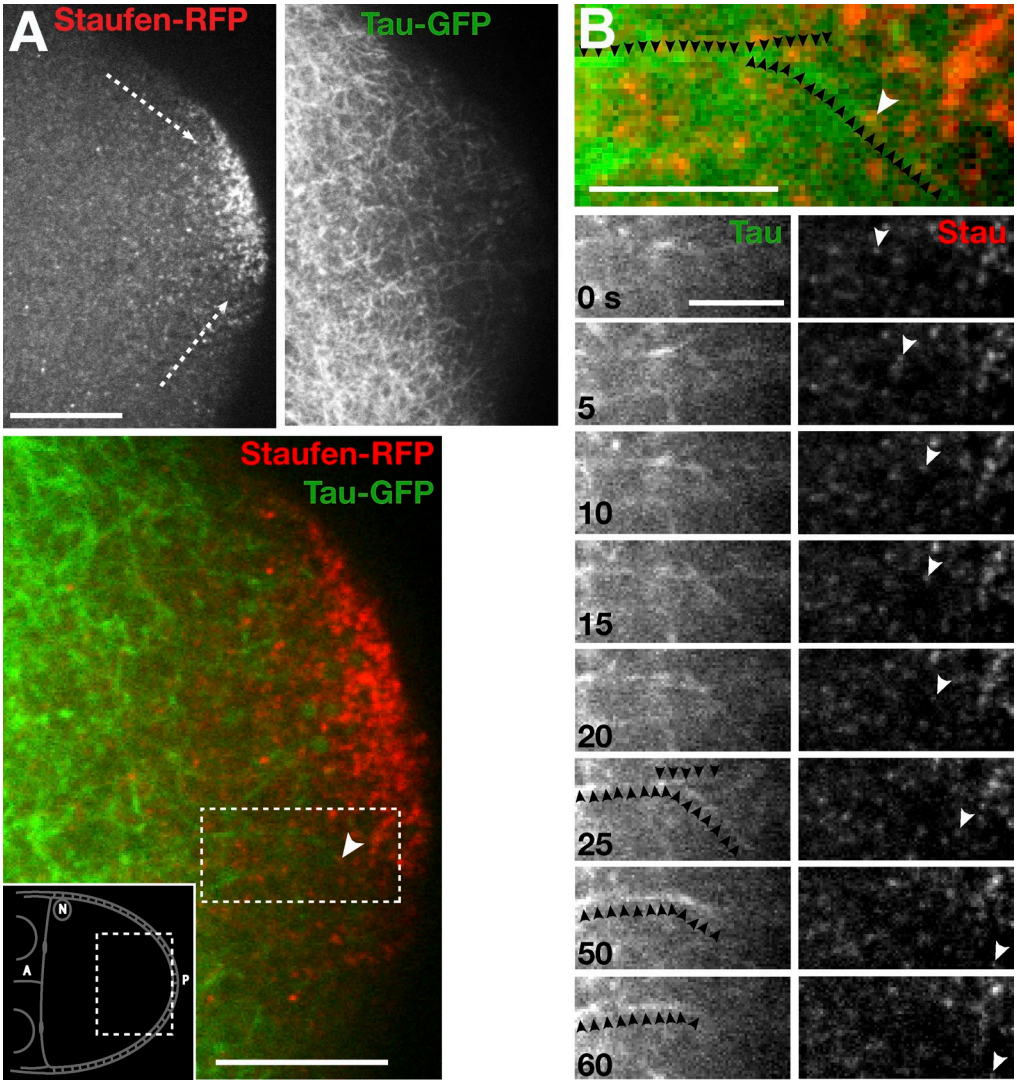

Figure 3. **Staufen protein is transported on MTs at the oocyte posterior.** Also see Fig. S1 and Video 4. (A) Dual-channel imaging of Staufen-RFP (A, left and bottom) and Tau-GFP (A, right and bottom). Dashed arrows indicate paths of cargo transit along the cortex. (B) A single Staufen particle moving on Tau-GFP–labeled MTs taken from the outlined region in A (bottom). (B, bottom) Time sequence of the particle (right, white arrowheads) moving in two runs along two different MTs (left, black arrowheads). The two MTs are indicated with arrowheads in the last three images to highlight the depolymerization of the lower one. A, anterior; P, posterior; N, oocyte nucleus. Bars: (A and C) 15 µm; (B) 7.5 µm.

are not in themselves sufficient to fully explain the stochastic nature of biased random cargo movements to the posterior (Zimyanin et al., 2008). Crucially, what is the underlying MT organization, and how does it account for the directional bias of cargo movements?

MT plus ends are organized in an anteroposterior gradient of orientation bias

Previous models for posterior cargo transport propose directed transport of cargoes away from the cortex (Cha et al., 2002) or directed transport on a MT cytoskeleton that is strongly polarized with the MT plus ends directed away from the anterior (Clark et al., 1994, 1997). Neither of these models explains the observed biased random cargo movements (Fig. 4 D; Zimyanin et al., 2008). A possible alternative model is that posterior biased random cargo movements are simply a reflection of an underlying biased random distribution of MT polarity in the oocyte. We tested this model directly using EB1-GFP as a reporter of the distribution and orientation of individual MTs throughout the oocyte as demonstrated in the first Results section (Fig. 2). Although individual tracks could be discerned by eye in a time-lapse video (Videos 2 and 3), it was not possible to determine global bias in the orientation of a field of MTs by manual inspection, necessitating the development of quantitative, automated methods. To our knowledge, there were no preexisting tools to analyze, plot, or characterize statistically MT orientation across a whole cell. Therefore, we developed new approaches to facilitate automatic tracking and quantify, statistically analyze, and display the ensemble polarity of EB1-GFP–labeled plus end trajectories. To achieve this, we first developed methods to effectively "extract" the moving components of an image sequence, to allow the dynamic EB1 foci to be robustly distinguished from the background in noisy image sequences

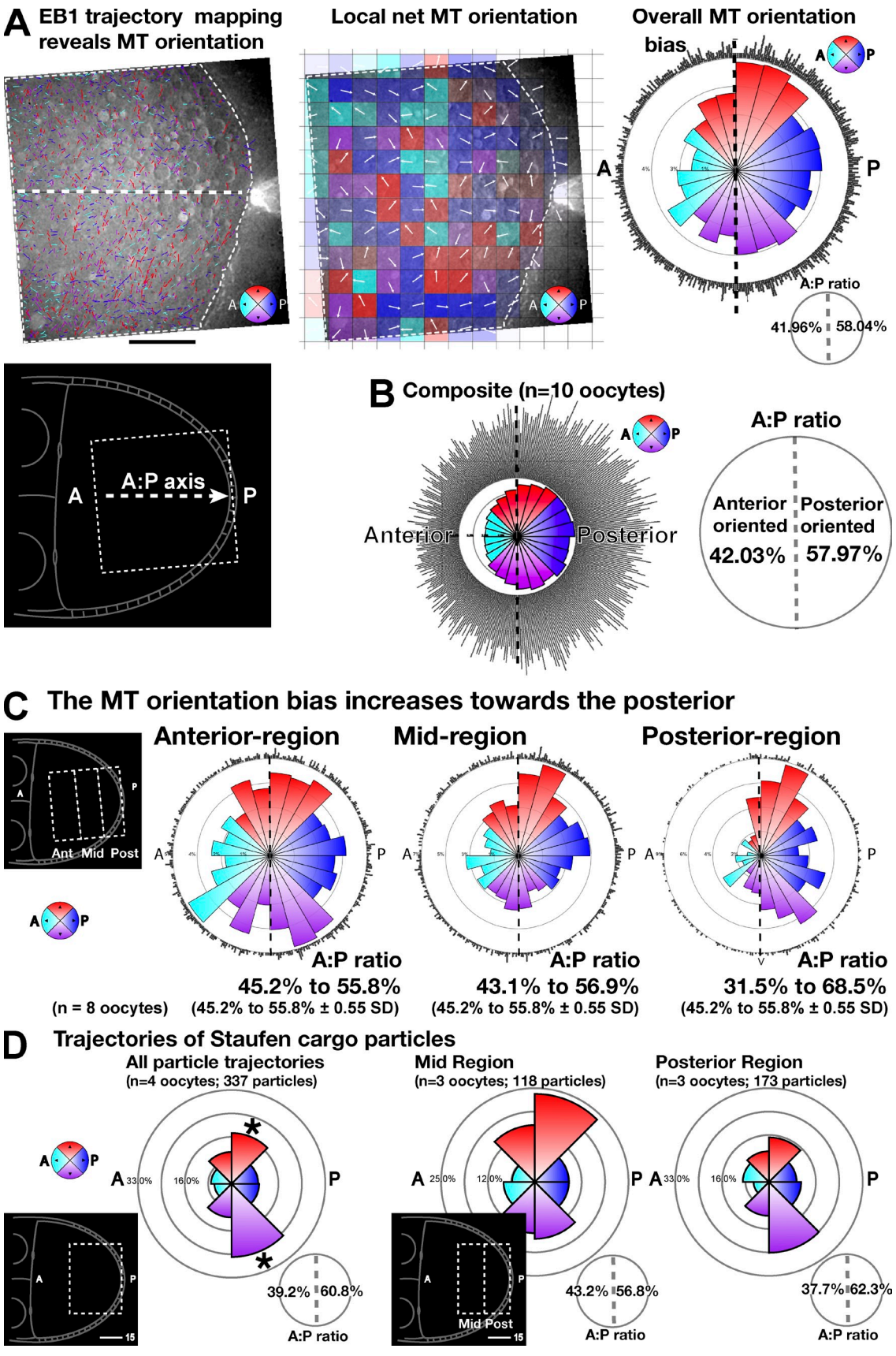

Figure 4. **Analysis of EB1 trajectories reveals a graded bias in MT orientation.** (A) Automatically tracked EB1 trajectories from a 120-frame video sequence imaged at three frames per second (fps; see Materials and methods; Fig. S2 and Fig. S3). The dashed white border indicates the track data plotted in the middle and right plots. Follicle cells are excluded. The central white dashed line indicates the anterior–posterior axis. The color of each track (refer to the

(see Materials and methods; Fig. S2). Probabilistic "soft segmentation" approaches were incorporated (Sharma and Aggarwal, 2010) to preserve image information. After these processing steps, automatic tracking was possible using conventional linkage analysis (Sbalzarini and Koumoutsakos, 2005; Yang et al., 2010) with minor modifications (see Materials and methods). We validated our automated tracking methods against manually tracked data, the so-called "ground truth" (see Materials and methods), and confirmed that we could accurately determine MT organization (Fig. S3).

Using these techniques, we assessed whether the dynamic MT network is organized in a biased random global orientation. Plotting individual MT trajectories (Fig. 4 A, left) highlights the apparent randomness of MT orientation. In contrast, calculating net local MT directionality across the oocyte (Hamilton et al., 2010) and displaying this as a windmap (Fig. 4 A, middle) revealed an overall subtle bias toward the posterior. To facilitate comparison of net orientation between different oocytes and to permit the display of pooled data from multiple oocytes, orientation data are summarized as a combined circular histogram and rose diagrams (Fig. 4, A [right, single oocyte] and B [pooled data for 10 oocytes]). For simplicity, the data are also summarized as the proportion of tracks oriented toward the posterior versus toward the anterior (Fig. 4, A [right, inset] and B [right]). This analysis revealed a consistent net overall bias of MT plus ends directed toward the posterior: 42.0% anterior to 58.0% posterior (n = 10 oocytes; Table I).

To determine how a dynamic MT network supports such an orientation bias, we assessed individual oocytes repeatedly at 15-min intervals (Fig. S4). We find that although small subregions show considerable variation in net orientation over time, which is consistent with a very dynamic network (Fig. S4, A and C, corresponding overlay of individual tracks), the overall bias is preserved (Fig. S4 B). Similar results were found for four oocytes (mean posterior bias of 59.3%; SD of 2.4%). We then tested whether MT orientation varies from anterior to posterior by defining and comparing regions of interest covering the anterior, mid-region, and posterior (Fig. 4 C, inset). We found that the strength of bias in MT orientation within the oocyte increases with distance from the anterior (Fig. 4 C), with a statistically significant stronger bias within 15 µm of the posterior cortex (36.9% anterior to 60.1% posterior; n = 8 oocytes; Table I).

To determine whether a random biased transport process acting on the dynamic MT network could quantitatively account for the observed movement of cargoes, we applied our novel global polarity visualization tools to quantitative analysis of Staufen-RFP trafficking. Our analysis revealed a statistically significant net bias in the direction in active transport of 39.2% anterior to 60.8% posterior (337 particle trajectories and four oocytes; χ^2 test, 99% confidence; Fig. 4 D). Comparison of regions at different distances from the posterior (Fig. 4 D, second and third plot and insets) shows that the bias in net movement is consistently stronger toward to posterior (62.3% posterior bias compared with 56.8% bias; n = 3 oocytes). Reexamination and statistical analysis of directionality for data from Zimyanin et al. (2008) showed general agreement with our current findings (Table I), although the bias toward the posterior was found to be less at the extreme posterior. This is likely to be a result of the inclusion of late stage 9 oocytes in the dataset, in which analysis of trajectories is hampered by the dense accumulation of fluorescent material at the posterior. Our results analyzing Staufen-RFP trafficking closely parallel the directional bias in MT organization and are entirely consistent with our model of the organization of the dynamic MT network underlying the observed transport. Collectively, these results demonstrate that a biased MT organization in the oocyte provides a good explanation for the movement of posterior-localizing cargoes through a biased random walk. Having determined the organization of the MT network in the oocyte, our findings raise the important questions what causes the bias in MT orientation, and how is this bias established and maintained?

A gradient in the density of MT initiation supports a net bias in MT orientation

To understand how the bias in MT polarity of the stage 9 oocyte is established and maintained, we first determined the distribution of γ-tubulin in the oocyte, previously used as a marker for the MT-organizing centers (Januschke et al., 2006). To maximize the contrast and detect fainter structures over the considerable background in the thick oocyte cytoplasm, we examined γ-tubulin37C–GFP distribution in live stage 9 oocytes using spinning-disc confocal microscopy. We find that, in addition to the previously described very bright foci associated with the nucleus (Fig. S5 A, middle, right, and bottom; Januschke et al., 2006), there are weaker foci distributed

color key on the bottom right), cyan, blue, red, or purple, corresponds to 90° ranges for anterior, posterior, dorsal, or ventral orientations. (bottom left) Inset shows the region of the oocyte imaged. (A, middle) Map of local net EB1 track orientation dividing the oocyte into 256 subregions. The color of each subregion is as described for A (left), although here, the net orientation of all racks crossing that subregion is indicated. The white arrow indicates the exact net orientation, whereas the density of color is proportional to the number of tracks for each subregion. (right) Summary of all orientation data from left plot. Combined circular histogram (outer dot plot indicating the orientation of each individual trajectory) and rose diagram (inner circular histogram plot of EB1 trajectories split over 24 15° ranges). The anterior versus posterior bias in orientation is also shown (bottom right) as the ratio of trajectories oriented within a 180° angle to the anterior (left of the dashed black vertical line) versus the 180° angle to the posterior (right). (B) Similar plots to those shown in A (right) summarizing data for 10 oocytes. (C) Plots comparing MT orientation for three adjacent 15-µm-wide regions of the oocyte at increasing distance from the posterior (left inset: anterior, mid, and posterior). (D) Manually tracked Staufen cargo movements in stage 9 oocytes. Particle trajectory orientations are plotted as rose diagrams with the proportion of particles trajectories shown in each of the eight 45° segments. The first rose diagram plots all moving cargoes in the posterior 30 µm (see inset). The second and third plots show subregions of 15 µm within the same area (see inset). The anterior versus posterior bias is shown as the ratio of trajectories oriented within a 180° angle to the anterior (left) versus the 180° angle to the posterior (right), confirming the bias in transport toward the posterior reported in Zimyanin et al. (2008). The dark asterisks on the first plot highlight the strong bias in the top and bottom posterior-directed segments, which can also be seen in the plots of MT orientation (A, right; and C, posterior region plot) and correspond to movements associated with MTs along the lateral cortex (highlighted in Fig. 3 A as dashed lines). A, anterior; P, posterior. Bars, 15 µm.

Table I. **Summary of tracking statistics**

Videos tracked	Ant/Post Bias		Deviation from random		Comparison (Watson test)
	Percent Ant (*n*)	Percent Post (*n*)	Rayleigh test		
	%	%			
Global EB1	42.0 (8,613)	58.0 (11,881)	1×10^{-133}	+++	Global EB1 versus Staufen: 0.001 < P < 0.01 (some similarity)
Global Staufen	44.1 (215)	55.9 (273)	3.2×10^{-4}	+	
par-1 EB1	49.4 (2,811)	50.6 (2,879)	2.5×10^{-3}	–	par1 versus global EB1: P < 0.001 (different to global EB1)
Global EB1[a]	42.0 (8,613)	58.0 (11,881)	1×10^{-133}	+++	
Ant EB1	46.4 (3,824)	53.6 (4,416)	1.7×10^{-10}	++	Ant versus mid: P < 0.001 (different)
Mid EB1	39.6 (2,188)	60.4 (3,341)	4.2×10^{-65}	+++	Mid versus post: P < 0.001 (different)
Post EB1	36.9 (1,466)	63.1 (2,506)	1.4×10^{-79}	+++	Ant versus post: P < 0.001 (different)
Ant EB1[a]	46.4 (3,824)	53.6 (4,416)	1.7×10^{-10}	++	

Ant, anterior; Post, posterior. In the Rayleigh test for uniformity of directional data, the degree of deviation from random is given (Mardia and Jupp, 2000). Results of the Rayleigh test are displayed on a scale from random (–) to not at all random (+++). In the Watson two-sample test for homogeneity of two samples of circular data, the higher the p-value, the more similar the populations (Mardia and Jupp, 2000).

[a]Duplicate data entries included to clarify the pairwise comparisons by Watson test.

along the anterior and lateral cortexes (Fig. S5 A). To test more directly whether, as suggested by the γ-tubulin distribution, MTs are nucleated at the anterolateral cortex, we performed MT depolymerization and regrowth experiments. Feeding flies with food containing colcemid (see Materials and methods), a potent inhibitor of MT polymerization, abolishes both Tau-GFP–labeled MT and EB1-GFP tracks in the oocyte, leaving persistent fluorescent foci along the anterior and lateral cortexes (Fig. 1 A and Fig. 5, A and B). We find that both Tau-GFP an EB1-GFP are present in foci at the anterolateral cortex (Fig. 5, A and B, respectively; and Fig. S5 B), whose density decreases markedly in a gradient toward the posterior (Fig. 5, B–B′′′′; and Fig. S5 B), but foci were not observed around the extreme posterior cortex (Fig. 5 B). Colcemid is known to shift the dynamic equilibrium of MT growth and disassembly toward depolymerization, leading to the shortening of MTs so that only short stubs of MTs remain at the site of initiation of MT growth. Therefore, we interpret our results as indicating that oocyte MTs are nucleated from the observed foci along the anterior and lateral cortexes.

To test directly whether MT growth from the anterior and lateral cortexes can give rise to the normal MT distribution in the oocyte, we inactivated colcemid with an exposure to UV light that is not harmful to oocyte viability (Theurkauf and Hazelrigg, 1998; Cha et al., 2002). It has been previously shown that UV inactivation of colcemid permits an MT network to reestablish and, as has been shown previously, this re-established network is competent to support MT dependent RNA transport (Cha et al., 2001). We found that immediately upon inactivation of colcemid, MT growth initiated strongly along the anterior and the lateral cortex. MTs were initiated from each of the persistent cortical foci in an undirected manner consistent with normal MT organization. (Fig. 5 A and Videos 6 and 7). Although no regrowth of MTs was observed from the extreme posterior cortex (Fig. 5 C), we showed earlier that some MTs appear to orient away from the posterior. This could be explained by our observations of MTs extending from more anterior regions and bending round on themselves (Fig. 2 C and Video 3). Our data account for the overall distributions of MT orientations as well as the orientation of cargo transported at the extreme posterior (Fig. 4, C and D), showing that the small proportion of "backwards" trajectories are, in fact, predominantly oriented at steep lateral angles. Collectively, the distribution of MT initiation sites along the anterolateral cortex, but not the posterior cortex, provides an explanation for the observed MT network with an excess of MT plus ends directed toward the posterior.

PAR-1 is required for the exclusion of MT nucleation from the posterior cortex that causes the posterior bias in MT polarity in the oocyte

PAR-1 N1S loss-of-function mutant oocytes have previously been shown to disrupt MT organization, leading to increased density of MTs at the posterior and mislocalization of *osk* mRNA (Doerflinger et al., 2006, 2010). To test whether PAR-1 is required for the establishment of the polarity bias in MT orientation, we examine the organization of MTs in the strong loss-of-function *par-1* allelic combination ($\text{par-1}^{6323}/\text{par-1}^{W3}$). In marked contrast to wild type, we found that in *par-1* mutant oocytes, EB1-GFP distribution shows a high density of MTs throughout the posterior with distinct EB1 foci of MT nucleation detectable around the posterior cortex (Fig. 6, A–C; and Videos 8 and 9). These sites extend MTs away from the posterior toward the anterior such that the MT plus ends in the posterior region are directed away from the posterior cortex, the opposite orientation to the wild type. Consequentially, we find that the net posterior bias of plus end trajectories was reduced or completely abolished in the mutant background: 49.4% anterior to 50.6% posterior ($n = 4$ oocytes; also see Table I and Fig. 6, D–F). The suppression of MT initiation at the posterior cortex accounts for the sharp falloff in MT density and distribution of polarity bias in the oocyte. Dual imaging of EB1-GFP and Staufen-RFP in the *par-1* mutant background confirmed that posterior cargo is mislocalized as previously

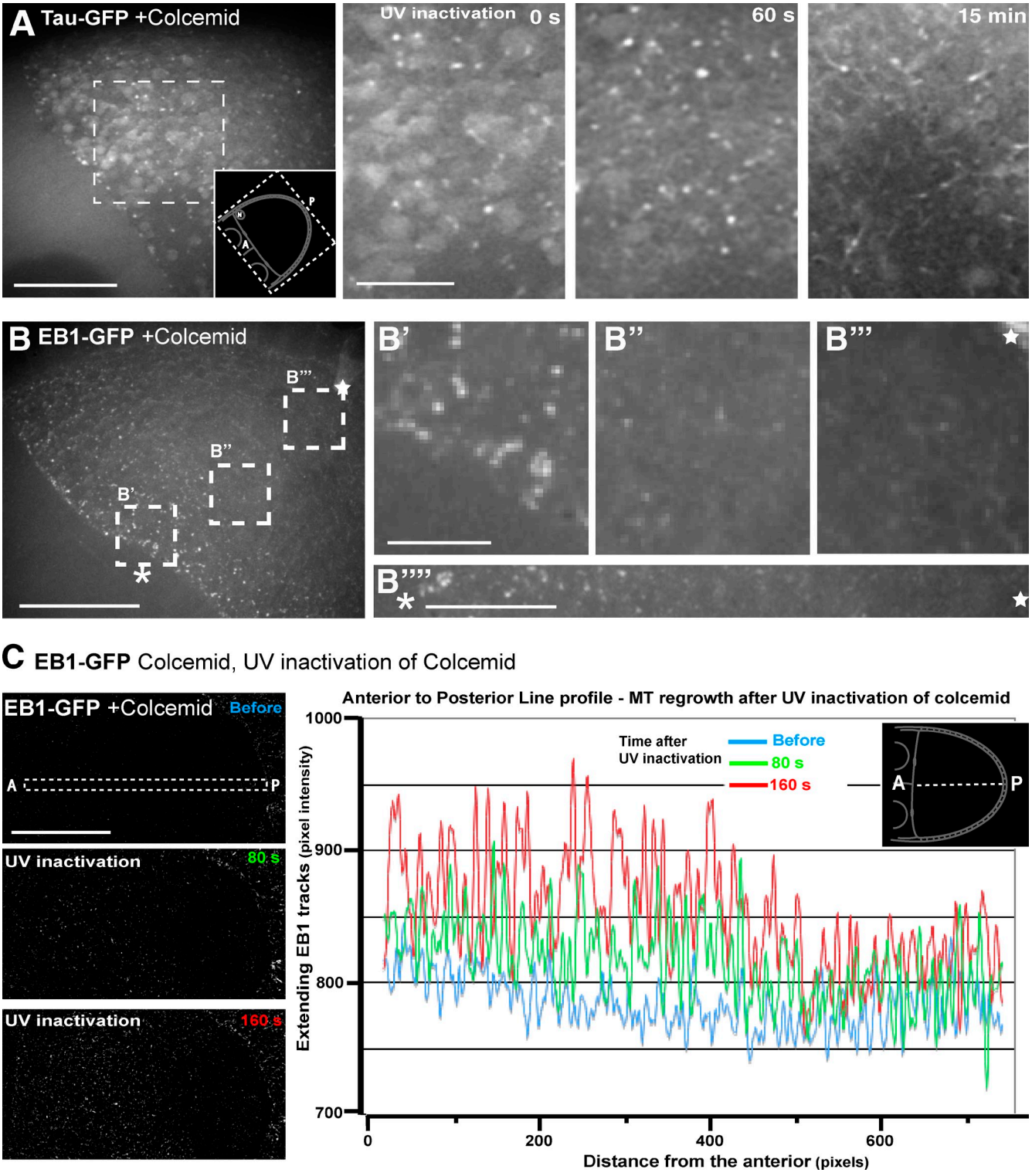

Figure 5. **MT nucleation occurs at discrete foci along the cortex but is absent from the posterior.** Also see Fig. S5 and Videos 6 and 7). (A) Tau-GFP–expressing oocyte treated with colcemid (see Materials and methods) showing the reduction of Tau-GFP MT labeling to small discrete foci; (right, first image) subregion of A shown enlarged; (second image) the same region after 60 s of UV inactivation protocol showing the initiation of MTs from the small foci; (third image) 15 min after UV inactivation showing extensive MT regrowth. (B) Oocyte expressing EB1-GFP similarly treated with colcemid revealing similar foci, which can be seen to distribute in a gradient of density from the anterior to posterior but appear to be absent from the extreme posterior (the extreme posterior is indicated by a star. (B′–B′′′′) Selected regions shown at increased magnification (highlighted in B and along a transect between the white asterisk and star). (C) Regrowth of MT after UV inactivation of colcemid assessed by the reappearance of EB1-GFP–labeled tracks (Videos 6 and 7) shows a lack of MT initiation from the posterior cortex. Images were foreground extracted (see Materials and methods) to identify actively extending EB1 tracks. Three time points are shown from the time sequence of UV inactivation of colcemid. For each image, a plot of pixel intensity from anterior to posterior is presented (corresponding to the region highlighted in the dashed box), relating to regrowth of MTs and revealing the restriction of MT initiation to the anterior regions. A, anterior; P, posterior; N, oocyte nucleus. Bars: (A–C) 20 µm; (A, right; and B′) 5 µm; (B′′′′) 10 µm.

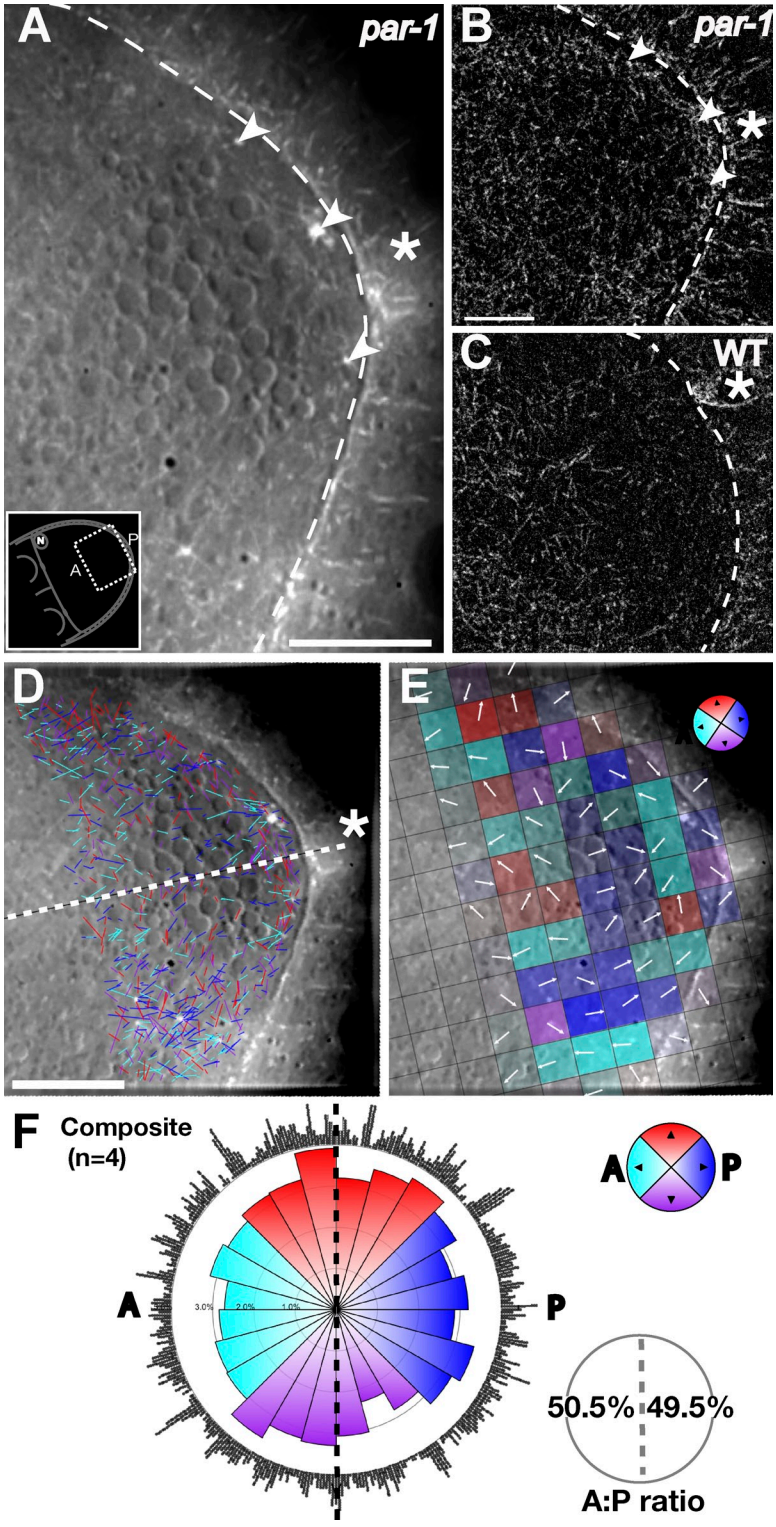

Figure 6. **MTs are nucleated around the entire posterior in *par-1* hypomorphic mutant oocytes, abolishing the orientation bias.** Also see Videos 8 and 9. (A) Trails projected EB1-GFP image time series. Arrowheads indicate EB1 foci nucleating MTs. The dashed line distinguishes oocyte and follicle cells, and an asterisk marks the posterior. (B) Image as in A after foreground extraction, highlighting EB1 foci nucleating MTs throughout the posterior. (C) Wild-type oocyte processed as in B showing the absence of MT initiating from the posterior cortex. (D–F) Mapping MT orientation in the *par-1* hypomorphic mutant: tracked EB1 trajectories, windmap, and rose diagram (refer to Fig 4 and Materials and methods for further details). A, anterior; P, posterior; N, oocyte nucleus. Bars, 15 µm.

described in *par-1* mutants (unpublished data), whereas time-lapse bright-field imaging revealed no obvious difference in cytoplasmic movements in *par-1* mutant oocytes compared with wild type (unpublished data). We conclude that the restriction of MT nucleation sites from the posterior cortex, as a consequence of PAR-1 action, is essential for the establishment and/or maintenance of the posterior bias in MT organization.

Discussion

Despite the importance of MTs in the oocyte, how they are organized and to what extent they are dynamic have remained highly controversial. Moreover, the prevailing models for MT organization have mostly relied on a static view of MT distribution and on indirect measures of polarity, such as the steady-state distribution of motor fusions and cargoes. By using live-cell

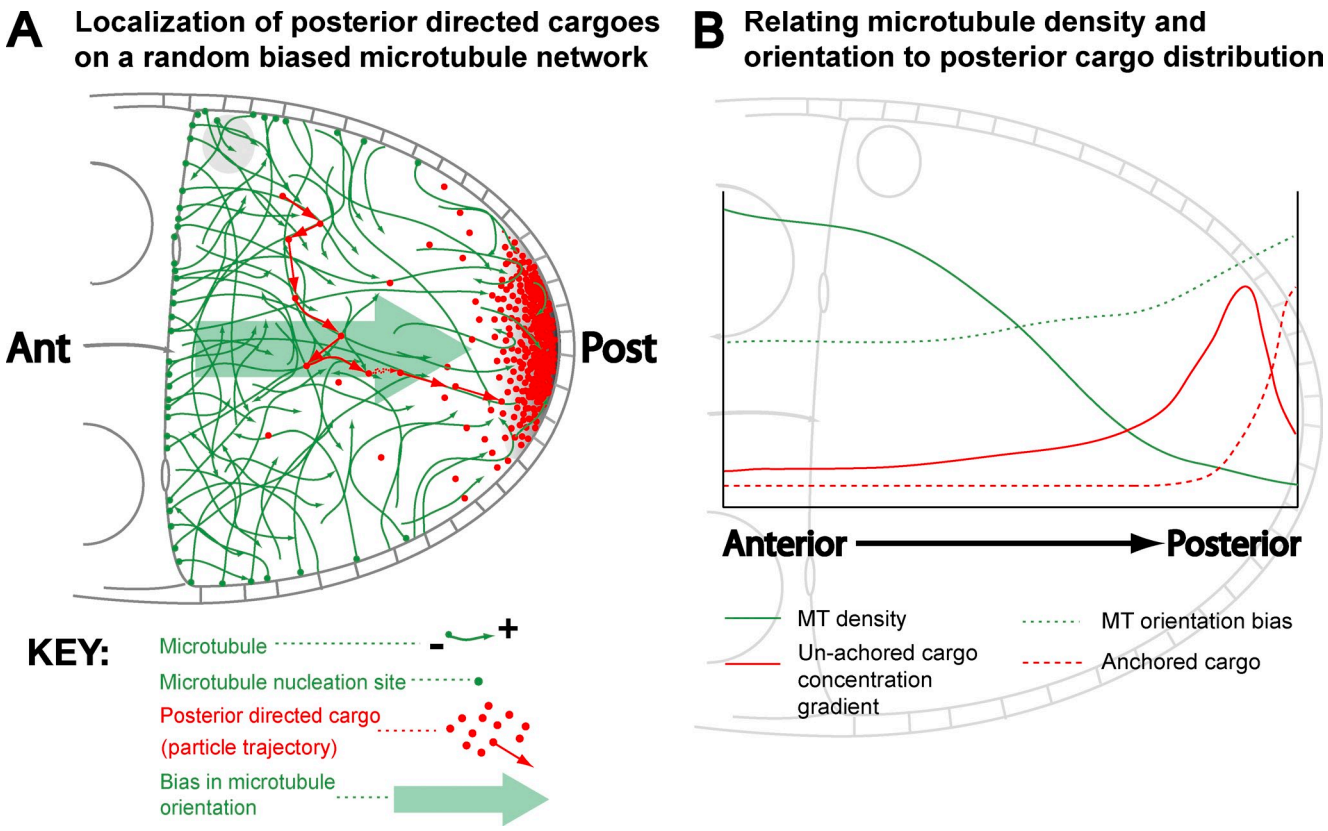

Figure 7. **A biased random organization of MTs in the oocyte delivers cargoes to the posterior.** (A) Interpretive model of biased random transport of posterior-localizing cargoes on a subtly polarized MT network. (B) Relating the distribution and orientation of MTs to the observed behavior of Staufen cargoes.

imaging and developing novel image analysis and global visualization tools, we have characterized directly the dynamics and polarity of MTs in living oocytes. We have found that MTs form a dynamic cortical network extending into the posterior with a bias in net orientation that increases toward the posterior. We have established that posterior-directed cargo is actively transported on these dynamic MTs, with no evidence for preferential transport by a subpopulation of more stable, posttranslationally modified MTs. Significantly, the magnitude and distribution of the observed bias in cargo movements parallels closely the polarity of the MT network. These findings explain the previously reported subtle biased random transport of posterior cargoes (Zimyanin et al., 2008) and lead us to propose the following model for posterior cargo localization: posterior cargo is transported on the entire dynamic MT network and the overall net bias in MT orientation directs the net movement of cargo to the posterior cap, where it becomes anchored (Fig. 7, A and B).

PAR-1–dependent exclusion of MT nucleation at the posterior of the oocyte establishes a biased MT network

Our results reveal that the establishment of the biased MT network is dependent on a specific distribution of MT nucleation sites around the oocyte cortex, with a critical, PAR-1–dependent exclusion of MT nucleation from the posterior cortex. This extends upon previous observations that PAR-1 affects MT organization, leading to an increased density of MTs at the posterior (Doerflinger et al., 2010). By using highly sensitive imaging techniques in live oocytes, we demonstrate that, in contrast to previous work (Januschke et al., 2006), in stage 9 oocytes, MT nucleation is also distributed along the anterior and lateral cortexes. Initiation of MTs is predominantly from the anterior of the oocyte with a sharp decrease in nucleation along the posterior two thirds of the oocyte cortex. Those MTs nucleating along the anterior are constrained to grow in a more posterior orientation, whereas nucleation along the lateral cortex is more random in orientation. The combination of these two contributions to the network of MTs present in the oocyte results in a slight excess of plus ends extending in a posterior direction, which increases in magnitude closer to the posterior. Despite the fact that, at the extreme posterior, there are no MT nucleation sites, we find that, even at the extreme posterior, a percentage of MTs appear to orient toward the anterior. We show that this is caused by MTs bending around as they extend into the posterior. Importantly, our detailed analysis of cargo movements reveals a bias in cargo movement directionality at the posterior that matches precisely the bias in MT orientation.

It is interesting to consider how the PAR-1 kinase might prevent the nucleation of MTs at the posterior cortex. The PAR genes are conserved polarity determinants with common functions in a variety of organisms (Shulman et al., 2000; Pellettieri and Seydoux, 2002). PAR-1 is known to function in association with other PAR proteins, so it is possible that the other PAR proteins also function together with PAR-1 to inhibit MT

nucleation in the oocyte. However, several other factors may also be involved. PAR-1 could affect MTs through its association with Tau, which has been shown in mammalian cells (Nishimura et al., 2004) and proposed in the *Drosophila* oocyte (Tian and Deng, 2009), but this remains contentious, as the presence of Tau is not absolutely required for PAR-1 function (Doerflinger et al., 2003, 2010). Another possibility is that PAR-1 could act through the components of the γ-TuRC complex or some other MT nucleation components, rather than through a direct affect on MTs. Whatever the molecular mechanism of PAR-1 inhibition of MT nucleation, it is most likely to involve the phosphorylation of a downstream target of the PAR-1 kinase.

A biased random dynamic network of MTs can perform multiple conflicting roles at a key developmental transition

Our live-imaging results highlight the role of a dynamic MT network in establishing cell polarity in the oocyte, in which we did not detect any stable, posttranslationally modified MTs. This raises the question of why this should be the case when, in some other cells, subsets of either stably bundled or completely stable, posttranslationally modified MTs have been observed and proposed to have functional roles in directing cell polarity (Li and Gundersen, 2008; Bartolini and Gundersen, 2010). Moreover, in many polarized cell types, including the blastoderm embryo and secretory columnar epithelial cells of egg chambers, MTs are organized with a very strong apical–basal polarity and include stable MTs. This makes functional sense in both cases, as cargoes have to be transported very rapidly either apically or basally. In contrast, in the oocyte, MTs perform three key functions that are not necessarily all compatible with having a very strict apical–basal polarity. First, they provide a means of randomly distributing generic components, such as mitochondria and lipid droplets, throughout the cytoplasm. Second, they provide a network to gather cargoes and redistribute them to distinct intracellular destinations, initiating and maintaining cell polarity. Third, they provide a scaffold that maintains structural integrity. We propose that the dynamic, subtly biased network of MTs in the oocyte provides an efficient compromise for dealing with these multiple conflicting biological requirements. During mid-oogenesis, the oocyte undergoes a huge expansion in size, when many cellular components are transported from the nurse cells or secreted from the overlying follicle cells. Although generic cellular components, such as Golgi, mitochondria (Hollenbeck and Saxton, 2005), and lipid droplets, must be kept distributed throughout the ooplasm (Herpers and Rabouille, 2004), the nucleus and specific mRNAs and proteins must be transported to different poles to establish the embryonic axes. A biased random network of MTs enables the mixing of generic components by continuous transport using molecular motors with opposing polarities, while, at the same time, allowing specific components to be transported by motors with single polarities to the anterior or posterior poles for anchoring. Furthermore, a network of highly dynamic MTs would allow efficient capturing of cargo by the motors throughout the entire ooplasm in a rapidly growing and developing oocyte. The fact that the MT network is highly dynamic also makes considerable functional sense for such a rapidly developing system. The MT cytoskeleton is reorganized extensively during *Drosophila* oogenesis but most dramatically during stage 7 (González-Reyes et al., 1995). This fits well with observations in other cell types showing that MTs are highly dynamic in nature and are often reorganized to direct cellular polarization (Mogensen et al., 2000; Etienne-Manneville and Hall, 2003; Jankovics and Brunner, 2006; Geraldo and Gordon-Weeks, 2009; Ohama and Hayashi, 2009; Bartolini and Gundersen, 2010).

Dynamic, subtly biased MT networks are likely to occur in many cell types

MTs certainly play critical roles in driving cell polarization and extension in many kinds of eukaryotic cells (Franz et al., 2002), for example, during guidance of extending neuronal growth cones (Geraldo and Gordon-Weeks, 2009), in migratory cells (Wood and Jacinto, 2007), in dorsal closure (Jankovics and Brunner, 2006), and in fields of bristles with planar polarity in fly wings (Lawrence et al., 2007). In all these cases, the polarity and dynamics of MTs have tended to be studied quite crudely because of an inability to follow the subtleties of global MT polarity and dynamics. Therefore, it is highly likely that MTs in such cells are more complex and subtle than previously thought. Interestingly, at least in *Xenopus laevis* oocytes in which hook decoration and EM were used as the previous gold standard for determining the polarity of individual MTs, a network of MTs is nucleated at the cortex, leading to a bias of polarity rather than an absolute polarity (Pfeiffer and Gard, 1999). Our methods are significantly easier to apply technically than hook decoration methods and are, therefore, more generally applicable to study the orientation and dynamics of MTs in most cells. For example, we have been able to apply our analysis tools to examine subtleties of MT organization in migratory border cells (unpublished data).

We propose that during cellular reorganization and repolarization, as in the oocyte, the establishment of a dynamic, subtly biased MT network is a widespread phenomenon and provides a general mechanism by which strong cell polarity can be initiated and maintained while efficiently handling the transport requirements of cargoes distributed throughout the cytoplasm. The tools we have developed to quantitate global or local bias in a complex field of MTs can now be applied widely to other oocytes and other cell types to test the generality of our proposed biased random model for MT organization.

Materials and methods

Fly strains

Stocks were raised on standard cornmeal agar medium at 21 or 25°C. MT markers used in this paper were EB1-GFP, EB1-mCherry expressed ubiquitously (provided by H. Okhura, Wellcome Trust Centre for Cell Biology, University of Edinburgh, Edinburgh, Scotland, UK), and Tau-GFP 65/167 (provided by D. St Johnston, University of Cambridge, Cambridge, England, UK). Posterior cargo markers used in this paper were *osk*:MCP-GFP, Staufen-RFP (provided by D. St Johnston), and γ-tubulin37C–GFP (provided by S. Endow, Duke University Medical Center, Durham, NC). PAR-1 mutant flies used in this study (provided by D. St Johnston) were w-;par-1[6323]/CyO and w-;par-1[w3]/CyO.

Tissue preparation and imaging

Flies were prepared, and ovaries were dissected and mounted for imaging as previously described in Parton et al. (2010). Imaging was performed either on a wide-field deconvolution system (DeltaVision CORE) from Applied

Precision (with a microscope [IX71; Olympus], 100× 1.4 NA objective, 16-bit camera [Cascade II; Roper Scientific], and standard Chroma filter sets), an OMX-V2 prototype microscope designed by J.W. Sedat (University of California, San Francisco, San Francisco, CA) and built by Applied Precision (Dobbie et al., 2010), or a spinning-disc confocal microscope (UltraVIEW VoX; PerkinElmer; with a microscope [IX81; Olympus], 60× 1.3 NA silicon immersion objective, and an electron-multiplying charge-coupled device camera [ImagEM; Hamamatsu Photonics]). Where required, image sequences were deconvolved with the SoftWoRx Resolve 3D constrained iterative deconvolution algorithm (Applied Precision). Basic image processing was performed with ImageJ (v1.43u; National Institutes of Health).

Immunofluorescence

Flies were prepared as previously described in Parton et al. (2010). Ovaries were dissected into PBS, pH 6.0, with 8% EM-grade PFA. After 5 min, ovaries were then transferred to 200 µl PBS, pH 7.0, with 8% EM-grade PFA, vortexed with 200 µl heptane to permeabilize the tissue, and fixed for a further 10 min. Immunofluorescence labeling was performed as in standard protocols (Cha et al., 2002; Rosales-Nieves et al., 2006). To detect tubulin modifications, we used antibodies, previously shown to work on *Drosophila* tissues, against acetylated tubulin (mouse monoclonal 6-11B-I; acetylated α-tubulin; Sigma-Aldrich) and glutamylated tubulin (clone 1D5 mouse hybridoma anti–Glu-α-tubulin; Synaptic Systems) at 1:250 and 1:300 dilutions, respectively (Warn et al., 1990; Januschke et al., 2006; Rosales-Nieves et al., 2006). Primary antibodies were applied overnight at 4°C. The secondary antibody donkey anti–mouse Alexa Fluor 594 (Invitrogen) was applied at 1:500 for 2 h at room temperature. The tissue was mounted in VECTASHIELD (Vector Laboratories) and imaged immediately by spinning-disc confocal microscope (UltraVIEW VoX).

Colcemid treatment

The protocol for colcemid feeding was modified from Cha et al. (2002): flies were fed for 1 d after eclosure, starved for 1 d, and then fed colcemid in yeast paste (200 µl of 0.1-mg/ml colcemid in distilled water added to 175 µl of dried yeast) for 4–6 h. Ovaries were dissected as normal.

Tracking and analysis

Through mid-oogenesis, the oocyte rapidly increases in size and accumulates yolk in the cytoplasm. This makes imaging increasingly challenging beyond stage 8. Furthermore, the EB1 protein is freely distributed in the cytoplasm as well as being associated with MT plus ends. This, combined with autofluorescence from the yolk, results in relatively poor contrast images of MT plus ends. Confocal methods increased contrast but proved insufficiently sensitive to detect the low EB1 signal. Wide-field deconvolution images were adequate for manual tracking of EB1 trajectories but resisted automatic segmentation and tracking without additional processing. For tracking analysis, oocytes expressing EB1-GFP were imaged on a wide-field deconvolution system (DeltaVision CORE) over three z planes twice per second with a pixel size of 97 nm. Image data were optionally denoised using the patch-based denoising algorithm ND-SAFIR (N-Dimensional–Structure Adaptative Filtering for Image Restoration; Boulanger et al., 2008) implemented in Priism (L. Shao, University of California, San Francisco, San Francisco, CA, and J.W. Sedat). Time series were deconvolved, the three z planes were maximally projected, and time points were equalized in SoftWoRx. Preprocessed image data were exported to 16-bit TIF format using ImageJ (64 V1.41) and imported into MATLAB (MathWorks).

To obtain statistically relevant data for EB1 track directionality, a robust automated tracking algorithm was developed that combined probabilistic foreground extraction and Haar-like feature identification (referred to here as probabilistic feature extraction; Fig. S4 and Fig. S5) implemented in MATLAB (v7.9). Probabilistic feature extraction and tracking comprises four components as follows: (1) local median equalization to correct for uneven illumination while preserving local contrast; (2) foreground extraction by a probabilistic temporal median filter to facilitate the discrimination of moving features from a static background; (3) identification of EB1 foci using Haar-like feature energy (adapted from Yang et al., 2010); and (4) linkage into trajectories using the particle-matching algorithm of Sbalzarini and Koumoutsakos (2005) with a modified cost function to take account of the linear path of EB1 tracks. For visual inspection, trajectories were output to a text file formatted for the ImageJ Manual Tracking plugin.

Local median equalization. To facilitate subsequent processing steps, all pixel values are normalized according to the ratio between the median for the local neighborhood (five times an EB1-GFP feature size, typically a 25 × 25–pixel patch) and the median for the whole image stack.

Probabilistic temporal median filter. To separate moving foreground features from the uneven static background, a probabilistic temporal median filter was devised. Using the median value of the neighboring few frames (where the number is defined here as W, as described in the following paragraphs) as a model for the static background has been proposed by several authors (Lo and Velastin, 2001; Cucchiara et al., 2003). Binary segmentation of pixels as either foreground or background throws away intensity information and is prone to error in the presence of noise. We therefore calculate a foreground probability image instead. We find that this soft segmentation preserves some of the original intensity information, facilitating subsequent processing steps.

For the entire normalized image sequence (from the Local median equalization section), a crude estimation of intensity variation caused by noise σ was made: for each pixel, the SD over the first W frames and the last W frames was calculated, and the mean of these values was taken as a measure of σ. W was chosen to be three times the mean time taken for an EB1-GFP particle to cross a pixel, typically $n = 15$.

The background intensity level, $I_{bg}(x,y,t)$, for each pixel at position x,y and time t was estimated by calculating the median over the surrounding W time points, i.e., from $t - 0.5 \times (W - 1)$ to $t + 0.5 \times (W - 1)$. The more the intensity value I(x,y,t) for a given pixel exceeds the static background value $I_{bg}(x,y,t)$, the more likely it is that a moving foreground feature (i.e., an EB1-GFP particle) is crossing the pixel. Instead of applying a binary cutoff, we therefore calculate a probability value P(x,y,t), which is the probability that the pixel is not a background feature:

$$P(x,y,t) = Q(-f) \tag{1}$$

in which $f(x,y,t) = [I(x,y,t) - I_{bg}(x,y,t) - k\sigma]/\sigma$ is the excess intensity above background normalized to 1 SD and $Q(f) = 0.5 \times (1 - \mathrm{erf}(f/\sqrt{2}))$ is the Q function, which is the tail probability of the standard normal distribution. Eq. 1 results in a foreground probability close to 1 when k = 0 and the intensity is 3 SDs or more above the background level. To produce a probability image in which the foreground features are not all saturated, k can instead be set to k > 0, and we find that a value of k = 1 produces satisfactory results for further analysis (Fig. S2 and Fig. S3).

Calculation of a particle probability image. Haar-like features were first used by Viola and Jones (2004) for face detection using a small number of critical features. A complex scheme for particle detection using Haar-like features was presented by Jiang et al. (2007), but for our foreground probability images, we find we are able to use a very simple segmentation criterion (adapted from Yang et al., 2010). Here, we calculate the energy for a single, square Haar-like feature representing a typical EB1-GFP particle (energy is calculated using pixel gray values as described in Yang et al., 2010; Eq. 1). For a particle of diameter 2w + 1, the half-width of the Haar-like feature window is w and the half-width of the internal feature is $w - 1$, in which a typical value of w is w = 2. The resulting Haar-like feature energy images can be rendered less noisy by application of one final filtering step: a particle probability score is calculated as a Gaussian weighted geometric mean of the highest Haar-like feature energy scores in the x,y,t neighborhood of each pixel. The neighborhood radius was set to v_{max} in x,y (v_{max} is the maximum velocity for a particle) and one time point about the current time point t. Segmentation of the resulting particle probability images can be achieved by applying a simple highest percentile threshold (T; normally $T \approx 1\%$ of the image area corresponds to EB1 foci) because the probability is highest when appropriately sized clusters of locally high intensity pixels persist within a distance v_{max} over multiple frames.

Trajectory determination. Trajectory determination was performed using the particle-matching algorithm of Sbalzarini and Koumoutsakos (2005) with a modified cost function:

$$\phi_{ij} = \delta(p_i, q_j) + \delta_{vec}(p_i, q_j) + \frac{1}{2}[(m_0(p_i) - m_0(q_j))^2 + (m_2(p_i) - m_2(q_j))^2],$$

$$\delta(p_i, q_j) = (\tilde{x}_{p_i} - \tilde{x}_{q_j})^2 + (\tilde{y}_{p_i} - \tilde{y}_{q_j})^2, \text{ and}$$

$$\delta_{vec}(p_i, q_j) = (\bar{x}_{p_i} - \bar{x}_{q_j})^2 + (\bar{y}_{p_i} - \bar{y}_{q_j})^2,$$

in which notation is as previously described in Sbalzarini and Koumoutsakos (2005), and the additional term δ_{vec} is the change in vector associated with linking point p_i with point q_i.

The validity of the automated tracking algorithm for determining EB1 track orientation was assessed by comparison with manually tracked data. The ground truth was determined by manually assigning the start and end points of all recognizable EB1 tracks over a 100-frame time series for both the "raw" time series data and the processed, segmented image data. Automatically determined and manually defined trajectories were plotted for comparison (Fig. S3, A and B).

To analyze the results of tracking, data were imported into the ParticleStats environment (Hamilton et al., 2010). ParticleStats directionality analysis tools were used to generate EB1 track overlays, net local directionality maps, rose diagrams, and radial histograms and to assess directional bias in EB1 tracks by the Rayleigh test of uniformity (assuming a circular normal distribution) and Watson two-sample test for comparing two samples of circular data (Mardia and Jupp, 2000). The validity of the automated tracking algorithm to report directionality was also assessed quantitatively by comparing the output from ParticleStats for the manual versus the automatic tracking data (Fig. S3 C).

Online supplemental material

Fig. S1 shows that MTs in the oocyte lack posttranslational modifications associated with increased stability (Fig. 2). Fig. S2 shows combined probabilistic foreground extraction and adaptive nonlocal means filter for automatic segmentation to detect EB1 tracks. Fig. S3 shows validation of automated detection and tracking of EB1 foci (see Materials and methods). Fig. S4 follows a MT over time showing that dynamic MTs support a consistent net bias in MT orientation (Fig. 4). Fig. S5 shows the distribution of γ-tubulin, supporting the idea that nucleation occurs at discrete foci along the cortex but is absent from the extreme posterior (Fig. 5). Video 1 shows a time series of Tau-GFP labeling dynamic MTs in the *Drosophila* oocyte (Fig. 1 B). Video 2 shows the localization of EB1-mCherry to the plus ends of Tau-GFP–labeled MTs. Video 3 shows EB1-GFP marking the plus ends of Tau-GFP–labeled MTs, revealing the highly dynamic nature of MTs in the oocyte (Fig. 2). Video 4 shows Staufen-RFP moving on Tau-GFP–labeled MTs at the posterior of a stage 9 oocyte. Video 5 shows a zoomed region with a single Staufen particle moving along an MT (Fig. 3 B). Video 6 shows MT regrowth from discrete foci after UV inactivation of colcemid. Video 7 shows a magnified view of individual EB1-labeled foci nucleating MT after UV treatment (Fig. 5). Video 8 shows "inappropriate" EB1-GFP–labeled foci nucleating MTs along the cortex of the extreme posterior in a *par-1* hypomorph (Fig. 6 A). Video 9 shows a magnified region of Video 8, highlighting individual EB1 trajectories. Online supplemental material is available at http://www.jcb.org/cgi/content/full/jcb.201103160/DC1.

We are especially grateful to Daniel St Johnston, Sharyn Endow, and Isabel Palacious for fly stocks and invaluable advice. Thanks also to David Finnegan, Tim Weil, John Sedat, and Dave Sherrat for advice and critical reading of the manuscript.

I. Davis, R.M. Parton, and R.S. Hamilton were funded by a Wellcome Trust Senior Fellowship to I. Davis (081858). L. Yang and G. Ball were supported by an Engineering and Physical Sciences Research Council grant (EP/F018673/1) to R.M. Parton, I. Davis, and W. Lu.

Submitted: 29 March 2011
Accepted: 7 June 2011

References

Bartolini, F., and G.G. Gundersen. 2010. Formins and microtubules. *Biochim. Biophys. Acta*. 1803:164–173. doi:10.1016/j.bbamcr.2009.07.006

Becalska, A.N., and E.R. Gavis. 2010. Bazooka regulates microtubule organization and spatial restriction of germ plasm assembly in the *Drosophila* oocyte. *Dev. Biol.* 340:528–538. doi:10.1016/j.ydbio.2010.02.006

Boulanger, J., C. Kervrann, J.-B. Salemero, and P. Bouthemy. 2008. Nonparametric regression for patch-based fluorescence microscopy image sequence denoising. *INRIA*. 6651:1–37.

Brendza, R.P., L.R. Serbus, J.B. Duffy, and W.M. Saxton. 2000. A function for kinesin I in the posterior transport of oskar mRNA and Staufen protein. *Science*. 289:2120–2122. doi:10.1126/science.289.5487.2120

Brendza, R.P., L.R. Serbus, W.M. Saxton, and J.B. Duffy. 2002. Posterior localization of dynein and dorsal-ventral axis formation depend on kinesin in *Drosophila* oocytes. *Curr. Biol.* 12:1541–1545. doi:10.1016/S0960-9822(02)01108-9

Cha, B.-J., B.S. Koppetsch, and W.E. Theurkauf. 2001. In vivo analysis of *Drosophila* bicoid mRNA localization reveals a novel microtubule-dependent axis specification pathway. *Cell*. 106:35–46. doi:10.1016/S0092-8674(01)00419-6

Cha, B.-J., L.R. Serbus, B.S. Koppetsch, and W.E. Theurkauf. 2002. Kinesin I-dependent cortical exclusion restricts pole plasm to the oocyte posterior. *Nat. Cell Biol.* 4:592–598.

Clark, I., E. Giniger, H. Ruohola-Baker, L.Y. Jan, and Y.N. Jan. 1994. Transient posterior localization of a kinesin fusion protein reflects anteroposterior polarity of the *Drosophila* oocyte. *Curr. Biol.* 4:289–300. doi:10.1016/S0960-9822(00)00068-3

Clark, I.E., L.Y. Jan, and Y.N. Jan. 1997. Reciprocal localization of Nod and kinesin fusion proteins indicates microtubule polarity in the *Drosophila* oocyte, epithelium, neuron and muscle. *Development*. 124:461–470.

Cucchiara, R., C. Grana, M. Piccardi, and A. Prati. 2003. Detecting moving objects, ghosts, and shadows in video streams. *IEEE Trans. Pattern Anal. Mach. Intell.* 25:1337–1342. doi:10.1109/TPAMI.2003.1233909

Czaplinski, K., and R.H. Singer. 2006. Pathways for mRNA localization in the cytoplasm. *Trends Biochem. Sci.* 31:687–693. doi:10.1016/j.tibs.2006.10.007

Dobbie, I.M., E. King, R.M. Parton, P.M. Carlton, J.W. Sedat, J.R. Swedlow, and I. Davis. 2010. OMX: a new platform for multimodal, multichannel wide-field imaging. *In* Live Cell Imaging: A Laboratory Manual. Second edition. R.D. Goldman, J.R. Swedlow, and D.L. Spector, editors. Cold Spring Harbor Laboratory Press, Cold Spring Harbor, NY. 203–214.

Doerflinger, H., R. Benton, J.M. Shulman, and D. St Johnston. 2003. The role of PAR-1 in regulating the polarised microtubule cytoskeleton in the *Drosophila* follicular epithelium. *Development*. 130:3965–3975. doi:10.1242/dev.00616

Doerflinger, H., R. Benton, I.L. Torres, M.F. Zwart, and D. St Johnston. 2006. *Drosophila* anterior-posterior polarity requires actin-dependent PAR-1 recruitment to the oocyte posterior. *Curr. Biol.* 16:1090–1095. doi:10.1016/j.cub.2006.04.001

Doerflinger, H., N. Vogt, I.L. Torres, V. Mirouse, I. Koch, C. Nüsslein-Volhard, and D. St Johnston. 2010. Bazooka is required for polarisation of the *Drosophila* anterior-posterior axis. *Development*. 137:1765–1773. doi:10.1242/dev.045807

Dunn, S., E.E. Morrison, T.B. Liverpool, C. Molina-París, R.A. Cross, M.C. Alonso, and M. Peckham. 2008. Differential trafficking of Kif5c on tyrosinated and detyrosinated microtubules in live cells. *J. Cell Sci.* 121:1085–1095. doi:10.1242/jcs.026492

Ephrussi, A., L.K. Dickinson, and R. Lehmann. 1991. Oskar organizes the germ plasm and directs localization of the posterior determinant nanos. *Cell*. 66:37–50. doi:10.1016/0092-8674(91)90137-N

Etienne-Manneville, S., and A. Hall. 2003. Cell polarity: Par6, aPKC and cytoskeletal crosstalk. *Curr. Opin. Cell Biol.* 15:67–72. doi:10.1016/S0955-0674(02)00005-4

Franz, C.M., G.E. Jones, and A.J. Ridley. 2002. Cell migration in development and disease. *Dev. Cell*. 2:153–158. doi:10.1016/S1534-5807(02)00120-X

Geraldo, S., and P.R. Gordon-Weeks. 2009. Cytoskeletal dynamics in growth-cone steering. *J. Cell Sci.* 122:3595–3604. doi:10.1242/jcs.042309

González-Reyes, A., H. Elliott, and D. St Johnston. 1995. Polarization of both major body axes in *Drosophila* by gurken-torpedo signalling. *Nature*. 375:654–658. doi:10.1038/375654a0

Hamilton, R.S., R.M. Parton, R.A. Oliveira, G. Vendra, G. Ball, K. Nasmyth, and I. Davis. 2010. ParticleStats: open source software for the analysis of particle motility and cytoskeletal polarity. *Nucleic Acids Res.* 38(Suppl. 2): W641–W646.

Hammond, J.W., D. Cai, and K.J. Verhey. 2008. Tubulin modifications and their cellular functions. *Curr. Opin. Cell Biol.* 20:71–76. doi:10.1016/j.ceb.2007.11.010

Herpers, B., and C. Rabouille. 2004. mRNA localization and ER-based protein sorting mechanisms dictate the use of transitional endoplasmic reticulum-golgi units involved in gurken transport in *Drosophila* oocytes. *Mol. Biol. Cell*. 15:5306–5317. doi:10.1091/mbc.E04-05-0398

Hollenbeck, P.J., and W.M. Saxton. 2005. The axonal transport of mitochondria. *J. Cell Sci.* 118:5411–5419. doi:10.1242/jcs.02745

Infante, A.S., M.S. Stein, Y. Zhai, G.G. Borisy, and G.G. Gundersen. 2000. Detyrosinated (Glu) microtubules are stabilized by an ATP-sensitive plus-end cap. *J. Cell Sci.* 113:3907–3919.

Jankovics, F., and D. Brunner. 2006. Transiently reorganized microtubules are essential for zippering during dorsal closure in *Drosophila melanogaster*. *Dev. Cell*. 11:375–385. doi:10.1016/j.devcel.2006.07.014

Januschke, J., L. Gervais, L. Gillet, G. Keryer, M. Bornens, and A. Guichet. 2006. The centrosome-nucleus complex and microtubule organization in the *Drosophila* oocyte. *Development*. 133:129–139. doi:10.1242/dev.02179

Jiang, S., X. Zhou, T. Kirchhausen, and S.T.C. Wong. 2007. Tracking molecular particles in live cells using fuzzy rule-based system. *Cytometry A*. 71:576–584.

Lawrence, P.A., G. Struhl, and J. Casal. 2007. Planar cell polarity: one or two pathways? *Nat. Rev. Genet.* 8:555–563. doi:10.1038/nrg2125

Li, R., and G.G. Gundersen. 2008. Beyond polymer polarity: how the cytoskeleton builds a polarized cell. *Nat. Rev. Mol. Cell Biol.* 9:860–873. doi:10.1038/nrm2522

Lo, B.P.L., and S.A. Velastin. 2001. Automatic congestion detection system for underground platforms. Proceedings of 2001 International Symposium on Intelligent Multimedia, Video and Speech Processing. 158–161.

Mardia, K.V., and P.E. Jupp. 2000. Directional Statistics. John Wiley & Sons Inc., New York/Chichester, England, UK. 429 pp.

Meignin, C., and I. Davis. 2010. Transmitting the message: intracellular mRNA localization. *Curr. Opin. Cell Biol.* 22:112–119. doi:10.1016/j.ceb.2009.11.011

Micklem, D.R., R. Dasgupta, H. Elliott, F. Gergely, C. Davidson, A. Brand, A. González-Reyes, and D. St Johnston. 1997. The mago nashi gene is required for the polarisation of the oocyte and the formation of perpendicular axes in *Drosophila*. *Curr. Biol.* 7:468–478. doi:10.1016/S0960-9822(06)00218-1

Mogensen, M.M., A. Malik, M. Piel, V. Bouckson-Castaing, and M. Bornens. 2000. Microtubule minus-end anchorage at centrosomal and non-centrosomal sites: the role of ninein. *J. Cell Sci.* 113:3013–3023.

Nishimura, I., Y. Yang, and B. Lu. 2004. PAR-1 kinase plays an initiator role in a temporally ordered phosphorylation process that confers tau toxicity in *Drosophila*. *Cell*. 116:671–682. doi:10.1016/S0092-8674(04)00170-9

Ohama, Y., and K. Hayashi. 2009. Relocalization of a microtubule-anchoring protein, ninein, from the centrosome to dendrites during differentiation of mouse neurons. *Histochem. Cell Biol.* 132:515–524. doi:10.1007/s00418-009-0631-z

Palacios, I.M., and D. St Johnston. 2002. Kinesin light chain-independent function of the Kinesin heavy chain in cytoplasmic streaming and posterior localisation in the *Drosophila* oocyte. *Development*. 129:5473–5485. doi:10.1242/dev.00119

Parton, R.M., A.M. Vallés, I.M. Dobbie, and I. Davis. 2010. Pushing the limits of live cell imaging in *Drosophila*. *In* Live Cell Imaging: A Laboratory Manual. Second edition. R.D. Goldman, J.R. Swedlow, and D.L. Spector, editors. Cold Spring Harbor Laboratory Press, Cold Spring Harbor, NY. 387–418.

Pellettieri, J., and G. Seydoux. 2002. Anterior-posterior polarity in *C. elegans* and *Drosophila*—PARallels and differences. *Science*. 298:1946–1950. doi:10.1126/science.1072162

Perez, F., G.S. Diamantopoulos, R. Stalder, and T.E. Kreis. 1999. CLIP-170 highlights growing microtubule ends in vivo. *Cell*. 96:517–527. doi:10.1016/S0092-8674(00)80656-X

Pfeiffer, D.C., and D.L. Gard. 1999. Microtubules in *Xenopus* oocytes are oriented with their minus-ends towards the cortex. *Cell Motil. Cytoskeleton*. 44:34–43. doi:10.1002/(SICI)1097-0169(199909)44:1<34::AID-CM3>3.0.CO;2-6

Reed, N.A., D. Cai, T.L. Blasius, G.T. Jih, E. Meyhofer, J. Gaertig, and K.J. Verhey. 2006. Microtubule acetylation promotes kinesin-1 binding and transport. *Curr. Biol.* 16:2166–2172. doi:10.1016/j.cub.2006.09.014

Rodriguez, A.J., K. Czaplinski, J.S. Condeelis, and R.H. Singer. 2008. Mechanisms and cellular roles of local protein synthesis in mammalian cells. *Curr. Opin. Cell Biol.* 20:144–149. doi:10.1016/j.ceb.2008.02.004

Rosales-Nieves, A.E., J.E. Johndrow, L.C. Keller, C.R. Magie, D.M. Pinto-Santini, and S.M. Parkhurst. 2006. Coordination of microtubule and microfilament dynamics by *Drosophila* Rho1, Spire and Cappuccino. *Nat. Cell Biol.* 8:367–376. doi:10.1038/ncb1385

Roth, S., F.S. Neuman-Silberberg, G. Barcelo, and T. Schüpbach. 1995. cornichon and the EGF receptor signaling process are necessary for both anterior-posterior and dorsal-ventral pattern formation in *Drosophila*. *Cell*. 81:967–978 (doi). doi:10.1016/0092-8674(95)90016-0

Sbalzarini, I.F., and P. Koumoutsakos. 2005. Feature point tracking and trajectory analysis for video imaging in cell biology. *J. Struct. Biol.* 151:182–195. doi:10.1016/j.jsb.2005.06.002

Serbus, L.R., B.-J. Cha, W.E. Theurkauf, and W.M. Saxton. 2005. Dynein and the actin cytoskeleton control kinesin-driven cytoplasmic streaming in *Drosophila* oocytes. *Development*. 132:3743–3752. doi:10.1242/dev.01956

Sharma, N., and L.M. Aggarwal. 2010. Automated medical image segmentation techniques. *J Med Phys*. 35:3–14. doi:10.4103/0971-6203.58777

Shimada, Y., S. Yonemura, H. Ohkura, D. Strutt, and T. Uemura. 2006. Polarized transport of Frizzled along the planar microtubule arrays in *Drosophila* wing epithelium. *Dev. Cell*. 10:209–222. doi:10.1016/j.devcel.2005.11.016

Shulman, J.M., R. Benton, and D. St Johnston. 2000. The *Drosophila* homolog of *C. elegans* PAR-1 organizes the oocyte cytoskeleton and directs oskar mRNA localization to the posterior pole. *Cell*. 101:377–388. doi:10.1016/S0092-8674(00)80848-X

Sousa, A., R. Reis, P. Sampaio, and C.E. Sunkel. 2007. The *Drosophila* CLASP homologue, Mast/Orbit regulates the dynamic behaviour of interphase microtubules by promoting the pause state. *Cell Motil. Cytoskeleton*. 64:605–620. doi:10.1002/cm.20208

Steinhauer, J., and D. Kalderon. 2006. Microtubule polarity and axis formation in the *Drosophila* oocyte. *Dev. Dyn.* 235:1455–1468. doi:10.1002/dvdy.20770

St Johnston, D. 2005. Moving messages: the intracellular localization of mRNAs. *Nat. Rev. Mol. Cell Biol.* 6:363–375. doi:10.1038/nrm1643

St Johnston, D., W. Driever, T. Berleth, S. Richstein, and C. Nüsslein-Volhard. 1989. Multiple steps in the localization of bicoid RNA to the anterior pole of the *Drosophila* oocyte. *Development*. 107(Suppl):13–19.

Tekotte, H., and I. Davis. 2002. Intracellular mRNA localization: motors move messages. *Trends Genet.* 18:636–642. doi:10.1016/S0168-9525(02)02819-6

Theurkauf, W.E., and T.I. Hazelrigg. 1998. In vivo analyses of cytoplasmic transport and cytoskeletal organization during *Drosophila* oogenesis: characterization of a multi-step anterior localization pathway. *Development*. 125:3655–3666.

Theurkauf, W.E., S. Smiley, M.L. Wong, and B.M. Alberts. 1992. Reorganization of the cytoskeleton during *Drosophila* oogenesis: implications for axis specification and intercellular transport. *Development*. 115:923–936.

Tian, A.-G., and W.-M. Deng. 2009. Par-1 and Tau regulate the anterior-posterior gradient of microtubules in *Drosophila* oocytes. *Dev. Biol.* 327:458–464. doi:10.1016/j.ydbio.2008.12.031

Viola, P., and M.J. Jones. 2004. Robust Real-Time Face Detection. *Int. J. Comput. Vis.* 57:137–154. doi:10.1023/B:VISI.0000013087.49260.fb

Warn, R.M., A. Harrison, V. Planques, N. Robert-Nicoud, and J. Wehland. 1990. Distribution of microtubules containing post-translationally modified alpha-tubulin during *Drosophila* embryogenesis. *Cell Motil. Cytoskeleton*. 17:34–45. doi:10.1002/cm.970170106

Weil, T.T., R.M. Parton, and I. Davis. 2010. Making the message clear: visualizing mRNA localization. *Trends Cell Biol.* 20:380–390. doi:10.1016/j.tcb.2010.03.006

Wood, W., and A. Jacinto. 2007. *Drosophila melanogaster* embryonic haemocytes: masters of multitasking. *Nat. Rev. Mol. Cell Biol.* 8:542–551. doi:10.1038/nrm2202

Yang, L., R. Parton, G. Ball, Z. Qiu, A.H. Greenaway, I. Davis, and W. Lu. 2010. An adaptive non-local means filter for denoising live-cell images and improving particle detection. *J. Struct. Biol.* 172:233–243. doi:10.1016/j.jsb.2010.06.019

Zimyanin, V.L., K. Belaya, J. Pecreaux, M.J. Gilchrist, A. Clark, I. Davis, and D. St Johnston. 2008. In vivo imaging of oskar mRNA transport reveals the mechanism of posterior localization. *Cell*. 134:843–853. doi:10.1016/j.cell.2008.06.053